PAPER

Check for updates

Electrochemical impedance spectroscopy-based screening of membrane effects *via* gas diffusion electrode half-cells for PEMFC performance optimization

Yawen Zhu, [ID] [a] Mena-Alexander Kräenbring, [ID] [a] Ivan Radev, [ID] [bc] Ahammed Suhail Odungat, [ID] [a] Lars Grebener, [ID] [a] Oliver Pasdag, [ID] [b] Thai Binh Nguyen, [d] Doris Segets [ID] [ae] and Fatih Özcan [ID] *[ae]

The widespread commercialization of polymer electrolyte membrane fuel cells (PEMFCs) is constrained by the performance and durability of the polymer electrolyte membrane, a critical bottleneck for gigawatt-scale technology. In traditional PEMFC setups with thin, reinforced membranes, the experimentally measured ohmic resistance (R_{ohm}) typically comprises contributions from contact resistances and high-frequency transport processes. Consequently, membrane thickness cannot be directly obtained as an independent resistance parameter in full-cell measurements. However, this study employed a gas diffusion electrode (GDE) half-cell setup combined with electrochemical impedance spectroscopy (EIS) and distribution of relaxation times (DRT) analysis to directly assess the membrane-related resistance. Under well-defined and reproducible conditions, this approach enables the separation and quantification of membrane- and interface-related contributions to ohmic, charge-transfer, and mass transport contributions. By comparing a GDE without membrane (true zero-thickness) as baseline to the extrapolated zero-thickness data, we quantify for the first time how membrane insertion itself reconfigures the catalyst layer (CL)/membrane interface, introducing a significant and fundamental baseline resistance. While our results confirm the established principle that total resistance (R_{total}) increases with membrane thickness, the initial membrane insertion – rather than thickness alone – is the primary driver of R_{ohm}. Conversely, membrane thickness is the key factor governing charge-transfer resistance (R_{ct}), whereas mass-transport resistance (R_{mt}) is fundamentally dictated by polymer chemistry and operating conditions. Beyond demonstrating the well-established GDE half-cell concept, this study establishes a quantitative, thickness-resolved framework for isolating and characterising membrane-induced resistances, offering mechanistic insights to guide rational membrane and electrode design for advanced PEMFCs.

a Institute for Energy and Material Processes – Particle Science and Technology, University of Duisburg-Essen, 47057 Duisburg, Germany. E-mail: fatih.oezcan@uni-due.de

b ZBT GmbH – The Hydrogen and Fuel Cell Center, 47057 Duisburg, Germany

c Institute of Electrochemistry and Energy Systems "Academician Evgeni Budevski", Bulgarian Academy of Sciences, 1113 Sofia, Republic of Bulgaria

d ICAN – Interdisciplinary Center for Analytics on the Nanoscale, 47057 Duisburg-Essen, Germany

e CENIDE – Center for Nanointegration, 47057 Duisburg-Essen, Germany

1. Introduction

The global transition toward carbon-neutral energy systems has driven rapid innovation in electrochemical conversion and storage technologies. Batteries provide highly efficient energy storage with rapid response but are constrained by low energy density and reliance on critical raw materials and thermal instability.[1] High-temperature fuel cells such as solid oxide fuel cells (SOFCs) provide excellent electrical efficiency and fuel flexibility, but their elevated operating temperatures lead to slow start-up and material degradation, restricting their application to steady-state power generation.[2] Other approaches, such as redox flow batteries, are primarily utilized for stationary energy storage systems, but their broader use is constrained by high system cost and maintenance requirements.[3] Among these, low-temperature fuel cells, particularly PEMFCs have emerged as a leading candidate to decarbonize key sectors of the economy, particularly in transportation and stationary power generation. Their unique combination of high power density, rapid start-up, near zero carbon emissions, and high electrical efficiency makes them a promising technology.[4,5]

At the heart of every PEMFC lies the MEA, in which the polymer electrolyte membrane (PEM) plays a crucial role: it enables selective proton transport while preventing fuel crossover, directly governing both efficiency and long-term durability. Because it is simultaneously responsible for both ion conduction and fuel separation, its gradual chemical and mechanical degradation is the primary driver of performance loss. These all make the membrane a critical bottleneck, where its properties directly govern the cell's immediate power output and its long-term viability. Improving membrane performance is therefore essential for advancing the PEMFC technology and securing its contribution to carbon-neutral energy systems.[6–8]

Developing an effective ion-exchange membrane is challenging, as it must exhibit high proton conductivity while retaining mechanical stability. The breakthrough in meeting this challenge came with the development of perfluorosulfonic acid (PFSA) ionomers, a class of materials whose success arises from their unique amphiphilic molecular architecture, consisting of a chemically inert, hydrophobic polytetrafluoroethylene (PTFE) backbone and side chains terminating in hydrophilic sulfonic acid groups. This structure induces nanoscale phase separation, creating continuous, water-filled hydrophilic domains that serve as proton-conducting pathways, while the hydrophobic matrix provides essential mechanical and chemical durability. This molecular design is realized mainly in two variants: long-side-chain (LSC) PFSA (commonly commercialized as Nafion) and short-side-chain (SSC) PFSA (commonly known as Aquivion). Other materials based on PFSA (such as partially fluorinated sulfonated polymers or mechanically reinforced PFSA membranes) also exist but are beyond the scope of this study. Notably, the shorter side chains in Aquivion increase sulfonic acid group density and polymer packing, resulting in higher proton conductivity under low humidity and improved mechanical strength compared to LSC ionomers.

But it has to be kept in mind that a membrane's performance is dictated by both its intrinsic polymer chemistry and its macroscopic form. Thereby, morphology governs the continuity of proton pathways, whereas reinforcement prevents swelling and increases mechanical durability. A key chemical parameter is the ion exchange capacity (IEC), which quantifies the density of sulfonic acid sites available for proton conduction. A higher IEC generally corresponds to a lower equivalent weight (EW), leading to improved proton conductivity and greater water uptake. This, in turn, reduces both the bulk protonic resistance and the local O_2 transport resistance within the cathode catalyst layer (CCL).[9–11]

Within this broader context, the physical thickness of the membrane acts as a key macroscopic design variable that directly impacts proton permeation and hence water formation, which further shapes the local electrochemical environment at the cathode. In principle, increasing membrane thickness increases the proton-transport path length and can increase the membrane-related ionic resistance. In practical PEMFC measurements, particularly with thin and reinforced membranes, the experimentally observed high-frequency resistance often also includes contributions from contacts and electrode

components (and unresolved very-fast processes). An increase in the apparent high-frequency resistance reduces the effective cathode potential under load. While thickness does not alter the intrinsic kinetics of the oxygen reduction reaction (ORR), the reduced effective cathode potential lowers the available overpotential window, thereby indirectly slowing the ORR rate. Furthermore, thickness dictates water management in a way that a thick membrane can impede product water removal, causing catalyst flooding and oxygen starvation, while a very thin membrane risks dehydration. Finally, thinner membranes permit higher hydrogen crossover, which consumes fuel, i.e., precious H_2, non-electrochemically and lowers the cathode potential. Therefore, optimizing a membrane is a multi-scale challenge that requires selecting the ideal molecular architecture (LSC vs. SSC) and then engineering its physical form factor (thickness) to achieve the optimal balance of competing ohmic, kinetic, and mass transport phenomena.[12]

Only few studies have managed to quantify how membrane thickness influences electrode performance, each having their own limitations. Most in situ investigations rely on conventional single-cell testing,[8,12–16] where the inherent complexity of the MEA makes it extremely challenging to decouple the membrane's contribution from other confounding factors, such as anode-side kinetics and hydrogen crossover.[17–19] This limitation prevents a clear attribution of performance changes to the membrane itself, thereby hindering rational design. Conversely, ex situ methods such as conductivity measurements provide only intrinsic material information and fail to capture the actual electrochemical environment in an operating fuel cell.[20,21] They neglect interfacial resistances between the CL and membrane, as well as gas transport effects and the coupling between proton conduction and the ORR, all of which critically determine device performance.[9,22–24]

A compromise solution to reduce complexity and at the same time investigate membranes in an application-relevant environment, could be half-cell testing. However, despite a significant amount of studies focusing on half-cell development itself and utilizing half-cell devices for rapid screening of material properties, no previous research has employed a GDE half-cell setup to isolate and investigate the specific contribution of the membrane under electrochemical operating conditions.[25–34]

To address this research gap, this study introduces an integrated methodology. We employ a GDE half-cell setup instead of traditional PEMFC single-cell to deliberately isolate the cathode, the primary site of performance limitation in PEMFCs thereby eliminating interferences from the anode,[27] and systematically examine membranes of different thicknesses and polymer chemistries: an ultra-thin SSC Aquivion Post Coat (4 μm in thickness) and FumaPem (15 μm), compared with LSC Nafion 211 (25 μm) and Nafion 212 (50 μm). To distinguish the membrane's role in a controlled way, we also include a GDE without a membrane, a so-called catalyst-coated substrate, as a zero-thickness reference. While this baseline does not reflect realistic PEMFC operation, it provides a meaningful academic benchmark to highlight and compare the incremental resistance and transport penalties introduced by the membrane

itself. Finally, to disentangle superimposed effects, we combine EIS with DRT analysis. EIS alone can quantify overall resistances, but it cannot unambiguously separate overlapping processes. DRT extends this capability by decomposing relaxation phenomena into distinct time domains, offering a clearer picture of how thickness alters proton transport, charge transfer, and diffusion resistances. This combined approach therefore provides more detailed mechanistic insight than conventional single-cell polarization or crossover tests.

The unique value of our study lies in this systematic, thickness-resolved characterisation. Building on the established GDE half-cell concept, we use GDE half-cells as a dedicated platform to isolate and quantify membrane-induced resistances under cathode-relevant conditions. The resulting data not only clarify how thickness governs fundamental processes underlying the ORR but also establish a practical evaluation routine for guiding future membrane and electrode design.

2. Experimental

The workflow of the electrode preparation and the followed electrochemical characterisation is shown in Fig. 1.

2.1 Materials

The catalyst ink was prepared following our previous work.[35] In brief, a commercial platinum catalyst supported on carbon black (approximately 50 wt% Pt, with an average particle size of approximately 5 nm) was used as active material. A PFSA solution was used as binder in dispersion. The ink formulation was adjusted to achieve a volumetric ionomer-to-carbon (I/C) ratio of 0.9. The solvent composition in the dispersion contained 30 wt% water and 70 wt% 1-propanol. The total solid content of the ink was maintained at 10 wt%. A detailed calculation of I/C ratio and the composition of the Pt/C catalyst is shown in SI 1.

The components were first mixed using magnetic stirring on a heated plate at 50 °C for 6 hours to ensure uniform dispersion. Following this, the mixture was subjected to high-shear homogenisation using a rotor-stator system (Kinematica Polytron, PT-DA 12/2 EC-F154) at 30.000 rpm for 10 minutes. A water-based cooling system was employed during homogenisation to maintain a constant temperature in the ink.

2.2 Electrode preparation

The catalyst inks were manually spray-coated onto a gas diffusion layer (GDL, H23C6, Freudenberg; thickness 250 µm) using an airbrush (ANEST IWATA Eclipse Takumi ECL-350T) positioned above a vacuum heating bed maintained at 90 °C (Fig. 1a). Airbrush spray coating is an established method for electrocatalytic layer fabrication and has been shown to provide good reproducibility when operated under controlled and standardized conditions.[36] In this work, a fixed coating protocol was applied following Kräenbring et al., including constant nozzle–substrate distance, spray pressure, ink flow rate, substrate temperature, and coating time. All electrodes were
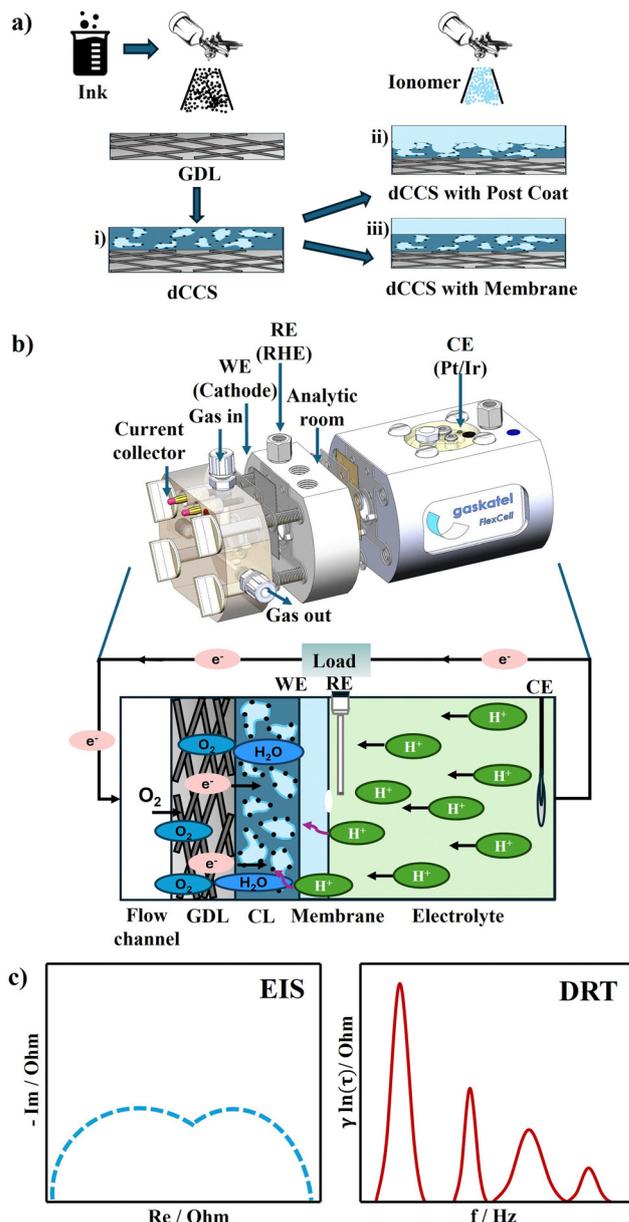

Fig. 1 Schematic illustration of the workflow. (a) Sample preparation that includes (i) the mere dCCS sample as a baseline, (ii) dCCS samples contacted with a spray-coated Aquivion Post Coat, and (iii) dCCS samples contacted with pre-hydrated commercial membranes; (b) electrochemical characterization using a GDE half-cell setup (the cross-section with membrane is only valid for the dCCS sample with membrane); schematic concept of data analysis using (c) EIS and DRT.

prepared using identical procedures to ensure comparability across samples. However, a statistically resolved thickness or roughness distribution was not the focus of the present study.[37]

The resulting electrode, referred to as a direct catalyst-coated substrate (dCCS, Fig. 1a, route i), served as the base GDE in this study and is denoted as 'dCCS without membrane' in Chapter 3. The platinum loading was controlled at a nominal value of 0.2 mg cm^{-2} by monitoring the mass change before and after coating.

Starting from this bare dCCS, two distinct electrode configurations were prepared and investigated separately. First, a thin ionomer layer was spray-coated directly onto the dCCS using the same PFSA solution as employed in the ink formulation, forming a post-coated electrolyte layer ('dCCS with Post Coat', Fig. 1a, route ii). This approach was chosen to ensure consistent ionomer chemistry across the CL and electrolyte interface. The thickness of the post-coated PFSA layer was approximately 4 μm, as determined by focused ion beam scanning electron microscopy (FIB-SEM) cross-sectional analysis at four different positions across the electrode surface (SI Fig. S1). The CLs exhibit reasonably uniform thickness with moderate local variations typical of manual spray coating, confirming the suitability of the preparation method for the comparative electrochemical analyses presented here.

In a separate sample configuration, commercially available proton exchange membranes were evaluated by assembling them onto the bare dCCS ('dCCS with Membrane', Fig. 1a, route iii). After removal of the protective film, the membrane was pre-hydrated for 2 h and subsequently assembled against the bare dCCS within the half-cell using a silicone sealing layer. No adhesive bonding or hot-pressing step was applied between the CL and the commercial membrane. The interfacial contact was established solely by mechanical compression in the half-cell. The key technical parameters of the three commercially available membranes, including thickness, IEC, and water uptake, are summarized in Table 1.[38,39]

2.3 Electrochemical measurements

Electrochemical characterisation was conducted using a Flexcell PTFE half-cell device from Gaskatel, which was connected to a Bio-Logic VSP-300 potentiostat. This setup, designed as a three-electrode system, is a key feature as it allows for precise control over the potential of the working electrode (WE) *via* the reference electrode (RE).[40] A hydrogen reference electrode (Mini-HydroFlex, Gaskatel) served as the RE, while a platinum/iridium (Pt/Ir) coil was used as the counter electrode (CE). During each measurement, the experimental geometry, contact conditions, electrolyte path, and electrode preparation are kept strictly constant, and only the membrane properties are varied. Under these controlled conditions, non-membrane-related contributions (GDL, CL, and contact resistances) are effectively invariant across samples, allowing thickness-dependent and membrane-induced effects to be resolved comparatively. A detailed cross-sectional schematic of the half-cell setup is shown in SI Fig. S2.

For each test, the electrode prepared as described in Fig. 1a was inserted between two custom-fabricated silicone gaskets and assembled into the test cell by tightening the four built-in screws of the Flexcell until the components were firmly sealed. This assembly method provides sufficient compression to ensure good interfacial contact, while avoiding excessive mechanical stress on the PTFE housing. The silicone gaskets confined the active WE area to 0.3 cm^2, which is significantly smaller than the CE area (3 cm^2). This large CE to WE area ratio minimizes potential gradients and ensures stable potential control.

As electrolyte, about 30 mL of a 1 M sulfuric acid (H$_2$SO$_4$) solution purchased from VWR Chemicals was used without further treatment. All potentials were recorded relative to a reversible hydrogen electrode (RHE) and all tests were performed at room temperature, with the cell open to the environment.

Prior to any measurements, the electrolyte was purged with Ar for 30 minutes to eliminate oxygen interference. The electrochemical cleaning of the cathode surface as described by Loukrakpam's work started with a cyclic voltammetry (CV) between 0.05–1.10 V at a scan rate of 500 mV s^{-1} until a stable voltammetric profile was achieved.[40] To evaluate the ORR activity, the potential was held at 0.1 V for 5 min in Ar atmosphere to pre-reduce the Pt surface. Then, first under Ar and subsequently under O$_2$ with a flowrate of 10 mL min^{-1} controlled by the digital flowmeter (Bronkhorst, D-6411), staircase potentio electrochemical impedance spectroscopy (SPEIS) was conducted. Thereby the voltage was decreased from 1 V to 0.2 V with an interval from 0.1 V with each voltage holding for 10 s. At the maximum current density observed in the polarization curve of the most active sample (≈ 550 mA cm^{-2}), this flow rate corresponded to an oxygen stoichiometric ratio of approximately 15. Hence, even under the most demanding conditions, the oxygen supply was in large excess, ensuring that mass transport was not limited by the external gas feed. Therefore, any mass-transport features observed in the impedance spectra can be attributed to internal resistances within the CL rather than to gas-feed limitations.

2.4 Electrochemical data analysis

Finally, EIS measurements were conducted at 0.6 V (ohmic polarization region) and at 0.3 V (mass transport polarization region) *vs.* RHE with a 5 mV amplitude across a frequency range of 30 kHz to 0.1 Hz to resolve R_{ohm}, R_{ct} and R_{mt}. A constant O$_2$ flow rate of 10 mL min^{-1} was supplied to the cathode through a calibrated flowmeter. The EIS data were processed using Bio-Logic EC-Lab software. The EIS data were then transformed to DRT function in eqn (1), where R_O (Ω) represents the ohmic resistance, $g(\tau)$ represents the time relaxation of the electrochemical reaction processes and f (Hz) represents the frequency:[41]

$$Z_{DRT}(f) = R_O + \int_0^\infty \frac{g(\tau)}{1 + i2\pi f\tau} d\tau \tag{1}$$

To account for the logarithmic distribution of frequency data in the impedance spectra and to enhance visualization,

Table 1 Technical data from the three commercial membranes used in this study: FumaPem, Nafion 211 and Nafion 212

Membrane type	Thickness (μm)	IEC (meq. g^{-1})	Water uptake (%)
Fumapem® FS-715-RFS	15	1.38	13
Nafion™ NR211	25	0.95–1.01	50
Nafion™ NR212	50	0.95–1.01	50

eqn (1) can also be rewritten in logarithmic scale:

$$Z_{\text{DRT}}(f) = R_O + \int_{-\infty}^{\infty} \frac{\gamma(\ln \tau)}{1 + i2\pi f \tau} d\ln \tau \tag{2}$$

where $\gamma(\ln \tau) = \tau g(\tau)$ and $\gamma(\ln \tau)$ represents the distribution function. For physical interpretation, the relaxation times (τ) obtained from the inversion are mapped to the frequency domain *via* eqn (3). Consequently, the results are plotted as $\gamma(\ln \tau)$ *vs.* the characteristic frequency f in the following analysis part, allowing for a direct correlation between DRT peaks and the frequency-dependent features observed in the Nyquist plots:

$$f = (2\pi\tau)^{-1} \tag{3}$$

During this work, the DRT was analysed *via* MATLAB R2023a and DRT webtools following the work by T. H. Wan *et al.*[41,42]

3. Results and discussion

3.1 Influence of membrane properties on overall performance

Understanding the context of a specific GDE configuration is essential before interpreting its electrochemical behaviour. Unlike a real PEMFC, the GDE allows measurements to be performed without a membrane, where the liquid electrolyte directly wets the CL and ensures efficient proton conduction and water removal. This environment represents an idealized condition for probing the ORR activity but does not fully capture the complexity of single-cell operation, where a polymer membrane acts as a solid electrolyte and water transport depends on diffusion and electro-osmotic backflow rather than direct removal by the liquid phase.

To comprehensively assess the impact of membranes with distinct properties on the GDE half-cell performance, it is essential to first evaluate how the presence and characteristics of the membrane influence the overall electrode performance. The polarization behaviour provides the most direct and crucial evidence of these effects, as it reflects how a single component – here, the presence of a membrane with distinct properties – modifies the ORR activity and overall cell efficiency. Therefore, it is important to begin the discussion with the polarization and power density curves to capture the macroscopic performance trends before employing impedance-based analyses to deconvolute how individual processes, such as charge transfer and mass transport, are affected by the membrane.

Fig. 2 compares the polarization and power density curves obtained using the GDE half-cell setup. To specifically isolate the impact of the membrane, all other experimental conditions were held constant so that the only free variable was the
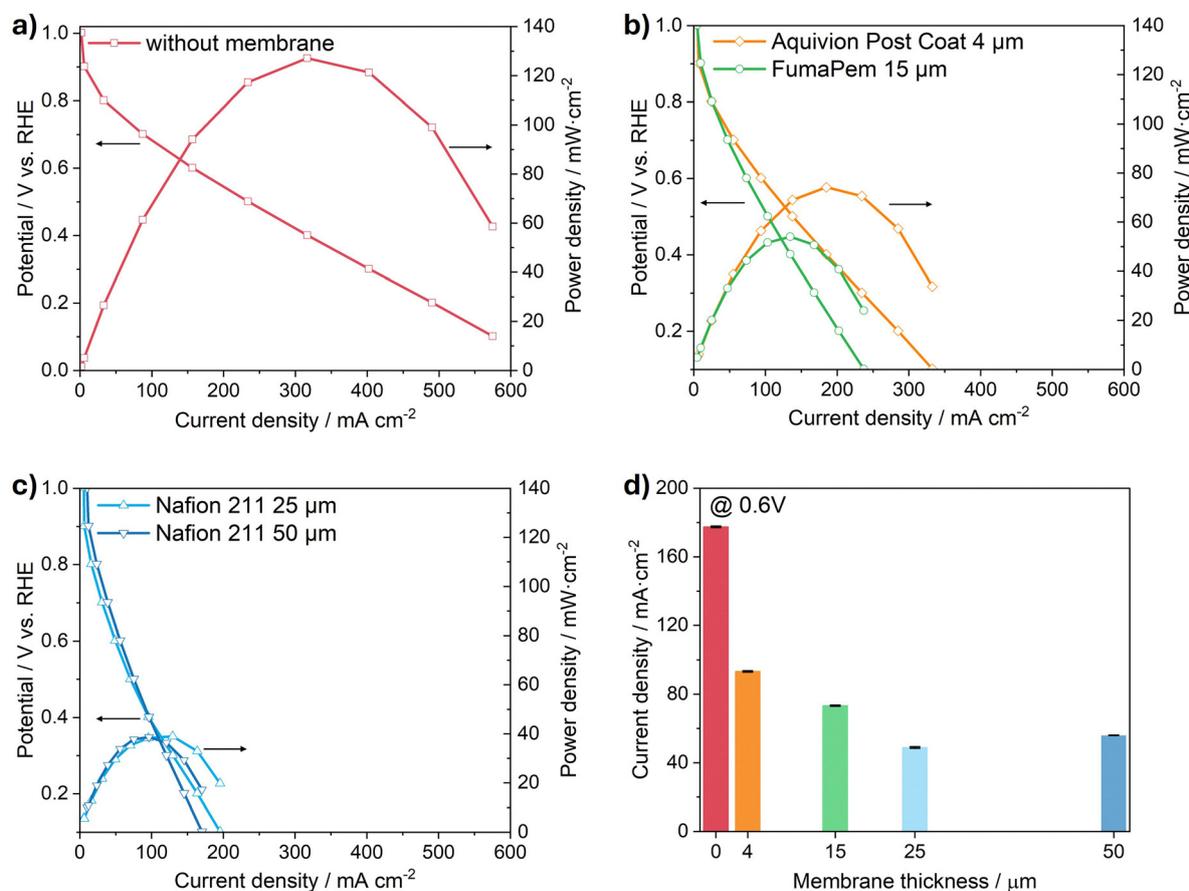

Fig. 2 Polarization and power density curves of GDE samples (a) without membrane, (b) with SSC Post Coat and membranes, (c) with LSC membranes, and (d) the current density from all samples at an operating voltage at 0.6 V.

presence and type of membranes in the different electrodes. The figure contrasts the performance of an electrode without a membrane (Fig. 2a), electrodes containing SSC ionomers (Aquivion Post Coat and FumaPem) (Fig. 2b), and with traditional laminated LSC membranes (Nafion 211 and 212) (Fig. 2c). A direct comparison of the electrode activity at 0.6 V is shown in Fig. 2d. The performance at 0.6 V was chosen as it provides a standardized measure of electrode activity under moderate load conditions. This potential lies in the kinetically controlled region for ORR in both half-cell and single-cell configurations, where mass-transport effects are limited but ohmic contributions become visible.[43] To verify that the comparatively low current densities observed in the half-cell configuration are not intrinsic to the catalyst formulation, selected electrodes were additionally evaluated in a conventional single-cell PEMFC under humidified reactants and elevated temperature. In this configuration, current densities of approximately 1.2 A cm^{-2} were achieved at 0.6 V, confirming substantially improved performance relative to the half-cell results. While this value remains below state-of-the-art PEMFC benchmarks, it suggests that the performance limitations observed in the present study primarily arise from the half-cell testing environment and, to some extent, from the current airbrush-based electrode fabrication process. In particular, partial pore blockage of the GDL during manual spray coating cannot be excluded and may hinder efficient gas transport at high current densities. Further optimization of the catalyst-layer deposition strategy is therefore required and will be addressed in future work.

As expected, the electrode measured without a membrane (Fig. 2a) exhibits the highest current density and peak power, reaching approximately 550 mA cm^{-2} and 120 mW cm^{-2}. This superior performance stems from the idealized three-phase boundary: oxygen flows directly to the CL, the liquid electrolyte maintains a well-humidified gas–liquid–solid interface, while simultaneously providing protons for the ORR. Under these conditions, ohmic and transport losses are minimal, and product water is efficiently removed into the bulk electrolyte.

By contrast, the introduction of a solid electrolyte in form of a polymer membrane (Fig. 2b and c) significantly reduces both current density and peak power. The SSC-type membranes (Fig. 2b) show an intermediate performance, while the LSC-type Nafion membranes (Fig. 2c) exhibit a further decline in current density and power density. A systematic trend is obvious from Fig. 2d, that is a significant decrease of activity as soon as a membrane as solid electrolyte is present (see the steep decline from 0 μm to 4 μm), and it continues to further decline from 4 μm to 25 μm. Interestingly, between 25 μm and 50 μm the current density levels off and stays nearly constant. These results demonstrate that the presence of a membrane layer strongly disrupts the liquid–solid–gas interface. After inserting the membrane, electro-osmotic drag pulls water from the electrolyte into the CL, where limited product removal can cause accumulation of water and finally flooding of the CL. As a result, performance declines, with thicker membranes shifting R_{ohm} upward and mass-transport limitations to lower currents.

The results indicate that the GDE half-cell does not reproduce the full operational complexity of a technical PEMFC. Accordingly, the aim of this study is not to benchmark absolute PEMFC performance, but to establish a comparative and internally consistent diagnostic framework for screening membrane- and interface-related transport effects. By preparing and testing all electrodes under identical conditions, the GDE half-cell enables systematic variation of membrane properties while preserving the validity of relative trends. Future work will extend this approach toward more application-relevant conditions, including humidified gas feeds and elevated temperatures.

To rationalize the performance differences observed in the polarization curves, the following section analyses the underlying electrochemical processes using EIS and DRT, allowing the individual contributions of charge transfer, proton conduction, and transport-related limitations to be distinguished.

3.2 In-depth electrochemical analysis *via* EIS

While the polarization curves capture the overall performance differences arising from the membrane, EIS measurements at 0.6 V (Fig. 3a) and 0.3 V (Fig. 3b) provide a more detailed perspective, resolving the influence of membrane thickness by separating it into distinct resistive and transport contributions. The Nyquist plots for the GDE without membrane (red symbols) and the Aquivion Post Coat (orange symbols) reveal only a single depressed semicircle across the entire voltage range. By contrast, electrodes with membranes (green: SSC, blue: LSC) display two well-defined semicircles. The first intercept with the real axis at high frequency corresponds to R_{ohm}, which includes both electronic and ionic contributions from the cell configuration and, most critically, from the membrane itself.[44] However, the subsequent semicircles associated with different ORR-related processes, such as reaction kinetics within the CCL and mass-transport limitations, cannot be clearly distinguished in the Nyquist plot and therefore require further analysis with respect to the different operating voltages.[12,45]

At higher operating voltages (Fig. 3a) (corresponding to medium current densities and near open circle voltage (OCV)), both the high-frequency intercept and the overall semicircle diameter increase with membrane thickness compared to the GDE without membrane, indicating a general rise in charge-transfer and diffusion resistance. The effect is most pronounced for the LSC-type Nafion membranes, particularly Nafion212 (50 μm), confirming that thicker and less hydrophilic membranes introduce higher ionic resistance and hinder proton transport across the interface. When the operating voltage decreases to 0.3 V (Fig. 3b), the impedance spectra show a noticeable reduction in total resistance compared to 0.6 V. The smaller semicircle diameters indicate faster charge-transfer kinetics under higher current densities. To address overlapping features in the Nyquist plots, the DRT analysis was applied for a more detailed interpretation.

3.3 In-depth electrochemical analysis *via* DRT

The DRT analysis (Fig. 4) converts the impedance spectra into frequency-dependent relaxation profiles, where overlapping
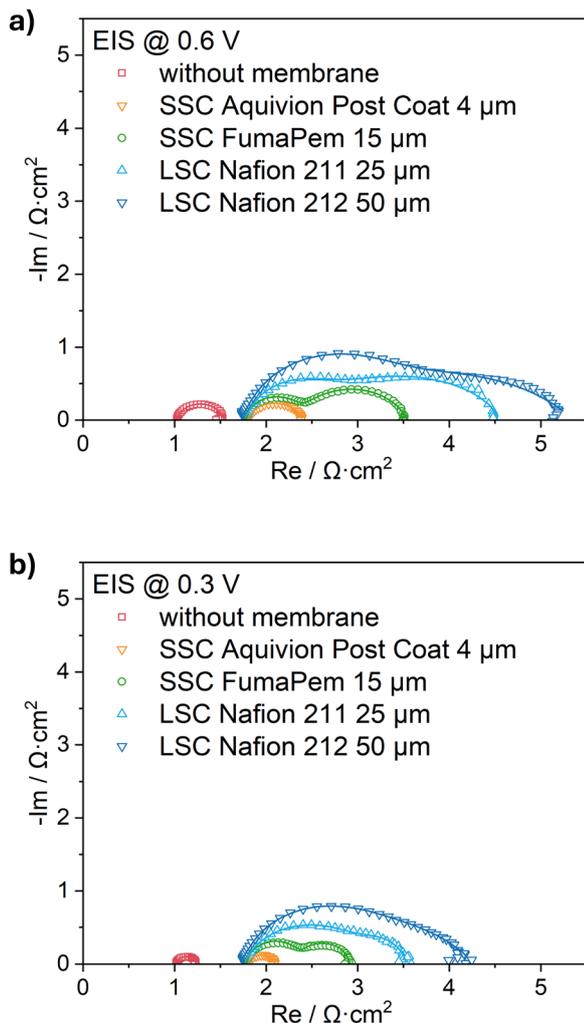
Fig. 3 Nyquist plot of EIS measured (a) at 0.6 V and (b) at 0.3 V for dCCS without membrane, with Aquivion Post-Coat and with PEM with different thickness (Fumapem, Nafion 211 and Nafion 212).

Fig. 4 DRT from the pure GDE without membrane and the corresponding GDEs with membranes of varying thickness (a) at 0.6 V and (b) at 0.3 V.

features appear as distinct peaks. This transformation allows for clearer separation and quantification of the ohmic, charge-transfer, and mass-transport processes that are otherwise convoluted in the EIS data.

To facilitate interpretation, we note that the DRT is plotted as a function of the relaxation time constant (τ), where each peak represents a dominant process within a characteristic τ (or frequency) window. In porous PEMFC electrodes, high-frequency features are typically dominated by predominantly ohmic and fast interfacial contributions, intermediate-frequency features are commonly associated with interfacial charge-transfer/double-layer processes of the ORR, and low-frequency features reflect slower transport-related phenomena in the porous electrode (e.g., gas transport and/or water-related limitations). In the present GDE half-cell, the absolute peak positions can additionally be influenced by the specific half-cell geometry (including electrolyte path length and separator interfaces). Therefore, we focus primarily on relative changes in peak intensity and position between separator configurations
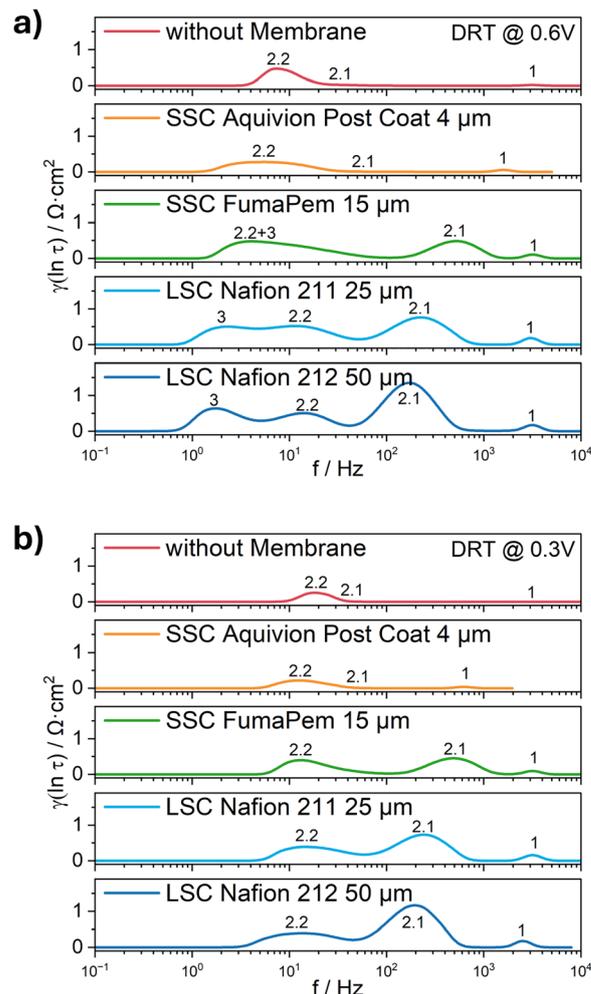
measured under identical conditions, and we use literature-supported assignments to discuss the most plausible physical origin of each peak.[46,47] A more detailed peak position assignment is shown in SI Fig. S3.

In the following, we use the peak labels as a guide: peak 1 (high frequency) is attributed to localized proton transport through the ionomer-film and associated interfacial charging contributions; peak 2.1 (intermediate frequency, observed here in the 200–600 Hz range depending on the membrane) is assigned to ORR charge-transfer kinetics; peak 2.2 (lower frequency, below 200 Hz) is associated with slower pseudocapacitive surface/adsorbate-related relaxations; and peak 3 (lowest frequency, when present) reflects a low-frequency transport-/wetting-state contribution (including water-management effects) (R_{mt}), typically linked to gas/water transport through the porous electrode structure. In this GDE half-cell, this low-frequency contribution is regime-dependent and is only clearly resolved at 0.6 V. At 0.3 V it is weak/not separable in the DRT within the measured frequency window, indicating that it should not be interpreted as a purely gas-diffusion peak across all conditions. A further possible reason is that the higher-current operating

point (0.3 V) may increase local heat generation and shift the cathode wetting state, potentially reducing liquid accumulation and suppressing a flooding-related low-frequency signature. This interpretation is proposed as a contributing hypothesis confirming it would require dedicated temperature/water management measurements.

DRT analysis across different membrane thicknesses, polymer properties and voltages reveals systematic changes in process contributions. At 0.6 V (Fig. 4a), the high-frequency peak (peak 1) becomes increasingly pronounced upon insertion of a membrane and continues to grow with increasing membrane thickness. The high-frequency response corresponds to a localized proton-transport (LPT) through-ionomer-film-process involving interfacial double-layer charging, which is characteristic of a small Maxwell–Wagner-type transmission-line relaxation.[48] The same tendency is also shown with the operating voltage at 0.3 V (Fig. 4b).

The intermediate-frequency peak (peak 2.1), which is correlated with the ORR charge-transfer kinetics occurring at the Pt active sites, remains weak in the electrode without a membrane and in the Aquivion post-coat sample, but becomes significantly more prominent with commercial membranes. This indicates that the integration of a commercial membrane introduces a measurable increase in the ORR electron-transfer resistance, likely by altering the physicochemical environment at the Pt–ionomer interface. Additionally, peak 2.1 shifts from ~600 Hz (FumaPem) to ~300 Hz (Nafion 211) and ~200 Hz (Nafion 212) as membrane thickness increases, reflecting the slower interfacial charging and proton-delivery kinetics introduced by thicker membranes.

Analysis of the intermediate and low-frequency regions in the DRT spectra, specifically focusing on peak 2.2 and peak 3, reveals significant differences in the electrochemical processes that are related to surface phenomena and gas diffusion across the various GDEs. Peak 2.2 is likely associated with slower pseudocapacitive phenomena at the Pt surface, such as the relaxation of oxygen- or sulfate-adsorbate coverage.[49] Peak 3, appearing at the lowest frequencies, reflects R_{mt}, which typically arises from gas diffusion through the porous CL and the GDL.

For the membrane-free sample and the post-coated Aquivion electrode, only peak 2.2 is observed, indicating the absence of a detectable mass-transport contribution. In contrast, for samples containing SSC Fumapem (15 μm) and LSC Nafion membranes (25 μm and 50 μm) both, peak 2.2 and peak 3 are present but partially overlapping. The separation becomes more pronounced for the thicker LSC Nafion membrane, suggesting enhanced decoupling of surface and diffusion processes. The SSC ionomer promotes more defined and better-connected hydrophilic channels, enhancing water management and further reducing mass-transport limitations.

At 0.3 V (Fig. 4b), the behavior deviates from the trends observed at 0.6 V. While peaks 2.1 and 2.2 remain essentially unchanged, the low-frequency diffusion feature (peak 3) is absent across all samples. This disappearance is specific to the GDE half-cell configuration. Unlike in a single-cell, operating near the

limiting current causes significant oxygen consumption and water production, both of which lead to noticeable mass transfer limitations.[8] The GDE half-cell setup offers direct gas access from the backside of the electrode, ensuring an oxygen stoichiometry far above the kinetic demand even at low voltages. As a result, oxygen availability at the CL is not rate-limiting. The presence of a diffusion peak at 0.6 V but not at 0.3 V can be attributed to the relative balance between reaction kinetics and transport. At 0.6 V, the current density is moderate, allowing subtle mass-transport processes (e.g., water removal and local pore saturation) to become detectable in the DRT response. In contrast, at 0.3 V the ORR rate is strongly kinetically driven, and the high reaction rate rapidly consumes oxygen without inducing measurable transport limitations because the supplied oxygen flux remains orders of magnitude higher than the demand. However, by revealing distinct relaxation features, the DRT results enable the selection and validation of more appropriate equivalent circuit models for subsequent EIS fitting and parameter extraction.

3.4 Combined EIS-DRT analysis: equivalent circuit models

To quantitatively evaluate the influence of membrane type and thickness on the different resistance components, the four main resistances – R_{ohm}, R_{lpt}, R_{ct} and R_{mt} – were extracted using the equivalent circuit models. Because EIS alone can suffer from overlapping features, the peak information obtained from DRT was used to guide the selection of a more reliable fitting model (Fig. 5a and b). The fitting results are summarized in Table 2 and plotted in Fig. 5c and d. In all cases, the high-frequency intercept is represented by an ohmic resistance R_Ω, which accounts for ionic conduction through the electrolyte or membrane, electronic resistance in the GDE substrate, and contact resistances. Following the ohmic contribution, the first resistive element R_1 together with its associated constant phase element (CPE) represents the high-frequency relaxation process arising from localized proton transport limitations within the ionomer network.

The subsequent parallel RC element $(R_{2.1}\|C_{2.1})$ describes the rapid ORR charge-transfer kinetics at the Pt active sites. The capacitance $C_{2.1}$ represents the idealized double-layer response at these kinetically active locations. A second parallel branch $(R_{2.2}\|Q_{2.2})$ is introduced to represent slower pseudocapacitive processes occurring at the catalyst surface with the non-ideal capacitive behaviour. A CPE is therefore used instead of an ideal capacitor to account for surface heterogeneity and distributed time constants within the porous CL. In the case of the dCCS sample prepared by manual airbrush coating, the rough catalyst surface and non-uniform ionomer distribution further enhance these non-ideal characteristics, justifying the use of a CPE in place of an ideal capacitor to more accurately capture the electrode interfacial response.

For measurements done at 0.6 V, the equivalent circuit is expanded by incorporating a third parallel branch $(R_3\|Q_3)$. The need for this additional element distinguishes the model in Fig. 5b from that in Fig. 5a.
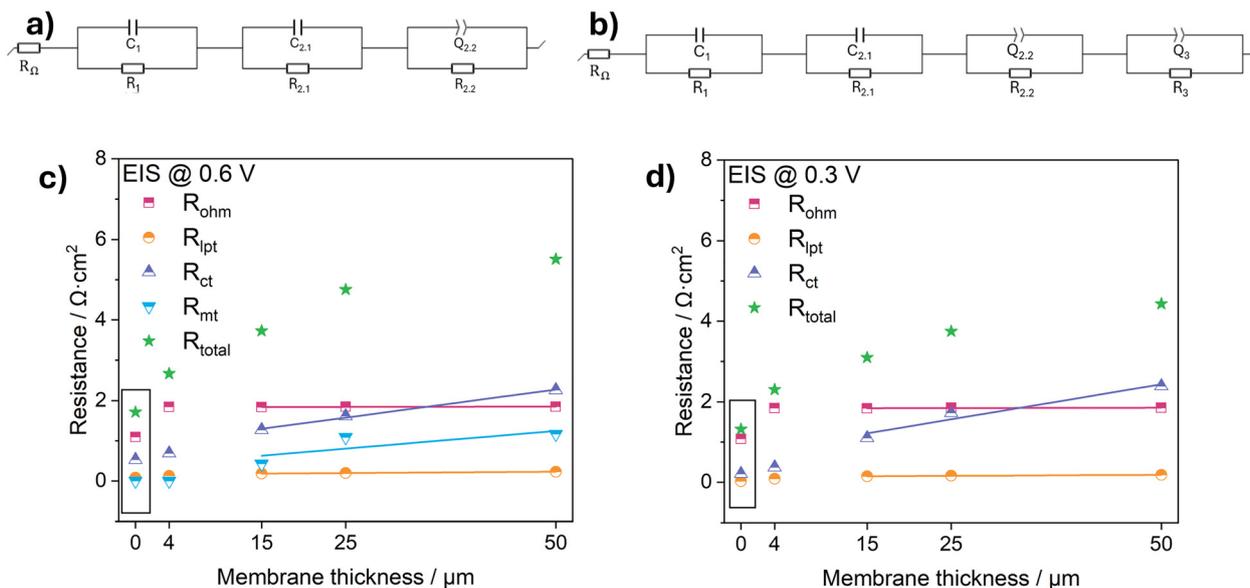
Fig. 5 Equivalent circuit models used for fitting the EIS data: (a) model without diffusion element and (b) model including the diffusion element. The extracted resistances (R_{ohm}, R_{lpt}, R_{ct} and R_{mt}) are shown together with linear fits for three membranes of different thicknesses at (c) 0.6 V and (d) 0.3 V.

Although transmission-line models (TLM) can in principle deconvolute distributed proton-transport and charge-transfer processes in porous CLs, they typically require additional assumptions and constraints to ensure parameter identifiability. In the present work we therefore employ a DRT-guided lumped-element equivalent-circuit model with the minimum number of parameters needed to describe the resolvable processes across all separator configurations. Within this framework, the resistance associated with localized proton transport in the ionomer network (R_1) is treated separately from the ORR R_{ct}, enabling a robust comparative analysis of membrane-induced changes. In the following section, the fitted parameters are evaluated with respect to membrane thickness and polymer chemistry.

3.5 Quantitative evaluation of membrane-induced resistance

After having defined the equivalent circuit models, the resistance values were obtained from each circuit element in the EIS fitting. The results are plotted as a function of membrane thickness in Fig. 5c and d (symbols) and summarized in Table 2. To relate membrane thickness and resistance with a physical model, we start from the following relation:

$$R = \rho \frac{l}{A} \quad (4)$$

Where ρ is the resistivity (Ω cm^2) of the material and is the inverse of conductivity k (S cm^{-1}). l is the length of the conduction path (cm) and is equal to the membrane thickness d here. Therefore, the membrane resistance R_{mem} can be written in:

$$R_{mem}(d) = \frac{1}{k} \cdot \frac{d}{A} \quad (5)$$

And the area specific resistance (ASR, Ω cm^2) can be written in:

$$R_{ASR}(d) = \frac{d}{k} \quad (6)$$

Thus, if the (ionic) conductivity k is constant, the R_{ASR} of the membrane is directly proportional to the thickness d:

$$R_{measured}(d) = R_{electrode} + R_{ASR} = R_{electrode} + \frac{d}{k} \quad (7)$$

From eqn (7) a linear relation between specific resistance and membrane thickness becomes apparent. To quantify this trend, linear regression was applied to each resistance component obtained from EIS fitting. The resulting fits were extrapolated toward the hypothetical case of an infinitely thin membrane. This has to be understood as an academic reference that, while not physically realizable, helps to isolate the intrinsic effect of membrane insertion on the overall resistance. The extrapolated values were then compared with the experimentally measured data for the pure GDE (without embrane), as summarized in Table 2 for 0.6 V and for 0.3 V, to assess the consistency of the model and identify the specific contribution of the membrane on the cell resistance.

3.5.1 Influence of membrane properties on ohmic resistance. The extrapolated R_{ohm} (Table 2) without a membrane is higher compared to the pure GDE configuration but similar to the results with the Aquivion post-coat and stays almost constant around 1.80 Ω cm^2 across all operating voltages and membrane thicknesses. The small variations are most likely due to a membrane-related interfacial series resistance that is largely thickness-independent. According to the technical data from FumaTech, the area resistance of FumaPem membranes

Table 2 Comparison of the extrapolated values with different membrane thickness to the values from the sample without membrane at 0.6 V and at 0.3 V

	0.6 V					0.3 V				
	Real resistance without membrane [R/Ohm cm^2]	Extrapolated value to zero membrane thickness [R/Ohm cm^2]	Slope of fitting	Real resistance with Post Coat at 4 µm [R/Ohm cm^2]	Extrapolated value with membrane thickness at 4 µm [R/Ohm cm^2]	Real resistance without membrane [R/Ohm cm^2]	Extrapolated value to zero membrane thickness [R/Ohm cm^2]	Slope of fitting	Real resistance with Post Coat at 4 µm [R/Ohm cm^2]	Extrapolated value with membrane thickness at 4 µm [R/Ohm cm^2]
R_{ohm}	1.095	1.835 ± 0.006	$3.462 \pm 1.945 \times 10^{-4}$	1.845	1.837 ± 0.006	1.081	1.839 ± 0.010	$-3.092 \times 10^{-4} \pm 3.091 \times 10^{-4}$	1.846	1.840 ± 0.010
R_{lpt}	0.086	0.167 ± 0.001	$0.001 \times 10^{-4} \pm 3.890^{-4}$	0.130	0.173 ± 0.001	0.028	0.137 ± 0.003	$9.676 \times 10^{-4} \pm 8.007 \times 10^{-4}$	0.087	$0.141 \pm 8.007 \times 10^{-4}$
R_{ct}	0.531	0.881 ± 0.063	0.028 ± 0.002	0.691	1.996 ± 0.063	0.212	0.695 ± 0.266	0.695 ± 0.266	0.373	0.835 ± 0.266
R_{mt}	0	0.366 ± 0.468	0.018 ± 0.14	0	0.436 ± 0.468					

in water at 25 °C is $< 0.04 \ \Omega \ cm^2$, which is orders of magnitude smaller than the observed $\sim 1.80 \ \Omega \ cm^2$. Consequently, the variation in R_{ohm} is governed not by the intrinsic through-plane resistance of the membrane, but by thickness-independent interfacial restructuring upon membrane insertion.

A comparison of the R_{ohm} for the extrapolated 4 µm-thick PEM and the Aquivion Post Coat electrode at both 0.6 V and 0.3 V (Table 2) further shows that their ohmic values are nearly identical. We interpret the data in a way that the increase in R_{ohm} arises from the cell configuration, where the insertion of a membrane creates additional interfaces such as CL/membrane contact regions and membrane/electrolyte boundaries, which introduce extra ionic contact resistances and wetting-related barriers that add to the measured ohmic contribution.

3.5.2 Influence of membrane properties on local proton transport resistance. The LPT contribution appears as a small, high-frequency peak that can be easily overlooked due to its low magnitude. The fitting results in Table 2 show that at both 0.6 V and 0.3 V the extrapolated LPT resistance at zero membrane thickness remains higher than that of the membrane-free GDE. This demonstrates that the insertion of the film itself introduces additional local proton transport resistance, even though this resistance is relatively small. Similar to R_{ohm}, this excess resistance is largely thickness-independent, suggesting an interfacial origin rather than a limitation by bulk membrane transport.

Notably, the Aquivion post-coated electrode exhibits a lower LPT resistance than the extrapolated zero-thickness value, demonstrating that this contribution can be partially mitigated through improved interfacial protonic coupling. This behavior indicates that LPT is governed by the local ionomer–CL interaction rather than membrane thickness alone. During the post-coating process, the PFSA solution can partially infiltrate into the upper region of the CL, leading to an increased local ionomer volume fraction and the formation of a graded interface.[50] This enhanced ionomer connectivity reduces the effective ionomer resistance at the interface and thereby mitigates interfacial proton transport losses, even at ultralow membrane thickness.

3.5.3 Influence of membrane properties on charge transfer resistance. The real and extrapolated R_{ct} at operating potentials of 0.6 V and 0.3 V are summarized in Table 2. For both the membrane-free GDE and the extrapolated zero-thickness values, R_{ct} is consistently higher at 0.6 V than at 0.3 V, indicating a systematic decrease in R_{ct} with decreasing operating potential. This behavior is in good agreement with literature, as higher current densities are associated with increased overpotential. This enhances ORR kinetics and lowers the apparent R_{ct} by facilitating electron–proton transfer at the catalyst surface.[12]

While this overall trend reflects improved kinetics at lower potentials, a clear discrepancy remains between the extrapolated zero-thickness values and the values determined for the true membrane-free GDE. Specifically, the difference between these two values increases from $0.35 \ \Omega \ cm^2$ at 0.6 V to $0.483 \ \Omega \ cm^2$ at 0.3 V. This growing deviation demonstrates

that the insertion of a membrane introduces an additional kinetic penalty that becomes more pronounced under high-current, high-proton-flux conditions. Even when extrapolated to zero membrane thickness, the presence of the membrane/CL interface fundamentally alters the local charge-transfer environment, highlighting the dominant role of interfacial effects beyond pure bulk transport.

The fitting results clearly demonstrate that R_{ct} increases almost monotonically with increasing membrane thickness, confirming that thicker membranes impose progressively larger kinetic penalties on the ORR. However, the magnitude of this increase is not governed by thickness alone. Membrane properties play a critical mitigating role: membranes that promote improved interfacial contact between the membrane and the CL can significantly reduce R_{ct} at a given thickness. This is evidenced by the post-coated membrane, which exhibits a substantially lower R_{ct} than the commercial membrane at comparable thickness, highlighting that enhanced membrane/CL interfacial connectivity can effectively suppress the thickness-induced increase in R_{ct}.

3.5.4 Influence of membrane properties on mass transport resistance. The mass-transport contribution is only observed at 0.6 V, where all electrodes incorporating a commercial PEM exhibit a distinct low-frequency feature (Fig. 4a, peak 3). In a liquid–electrolyte GDE half-cell, the local water/electrolyte distribution in the porous electrode can influence both kinetics and transport. While moderate interfacial wetting can improve ionomer hydration and proton access, excessive liquid water accumulation can restrict gas pathways and appears as an increased low-frequency transport contribution (peak 3 – R_{mt}). In this study we do not directly quantify electrolyte penetration depth into the CCL/GDL. Therefore, we emphasize separator-dependent trends under identical conditions. Notably, the ultrathin PFSA Post Coat exhibits a strongly reduced transport feature, consistent with improved interfacial proton access without a significant transport penalty, whereas thicker commercial membranes – particularly Nafion – show an increased peak 3 – R_{mt}, consistent with enhanced transport limitation *via* water retention near the cathode interface rather than bulk electrolyte crossing through the membrane.

At lower potentials, the characteristic time constants of transport/wetting processes may shift to very low frequencies and/or overlap with other low-frequency phenomena, so that a distinct maximum is not resolved by the DRT under our measurement conditions. We therefore focus on separator-dependent trends where the feature is reliably resolved (0.6 V) and discuss peak 3 as a transport-/water-management-related contribution rather than a pure gas-diffusion resistance.

As membrane thickness increases, the magnitude of R_{mt} becomes more pronounced, reflected by a higher peak intensity. In a GDE half-cell setup, at low currents the transport rates of reactants and products are slow leading to the formation of concentration gradients. This causes diffusion through the CL to become the rate-limiting step. As the current density increases, the rapid depletion of reactants enhances mixing effects, optimizing the transport of reactants through the flow field or electrolyte. This reduces mass transfer resistances within the system.[31]

While membrane thickness influences the magnitude of R_{mt}, polymer chemistry plays a more decisive role. For the SSC Aquivion Post Coat, the mass-transport peak nearly disappears, whereas for the SSC Fumapem membrane only a weak, partially overlapping feature remains. The deviation of the slope from the fitted R_{mt} values further confirms this: the thickness dependence is weak and shows larger scatter compared to the R_{ct}, indicating that mass-transport behavior is less governed by PEM thickness and more strongly determined by membrane chemistry. This becomes especially apparent for LSC Nafion 211 and 212, where R_{mt} rises sharply, highlighting that polymer backbone structure and hydration behavior strongly modulate diffusion limitations.

These differences can be rationalized by considering how each material interacts with the liquid electrolyte environment in the GDE half-cell. The 1 M H_2SO_4 electrolyte continuously supplies water to the CL/membrane interface. Membranes with high IEC, such as Fumapem, can therefore form highly connected proton-conducting domains without requiring substantial bulk swelling. Their lower water uptake minimizes pore flooding and preserves open gas pathways. In contrast, the higher water uptake of LSC Nafion leads to significant swelling, generating larger water-rich regions that obstruct gas pathways and increase tortuosity within the CL/GDL. This promotes local flooding and thick hydration layers at the triple-phase boundary, ultimately elevating R_{mt}.

Even though the operating situation at a GDE half-cell setup is completely different than that in the single-cell setup, it can give important mechanistic insight into the CL/ionomer membrane interplay by decomposing the total resistance into ohmic, localized proton-transport, charge-transfer, and mass-transport components. The combination of EIS and DRT enables to understand performance-limiting contributions and helps uncover which process dominates when a membrane of a specific thickness or chemistry is introduced. By decoupling CL and membrane effects, which is however not possible in the single-cell setup, it can be evaluated if mass-transport losses are rather originating from electrode-related parameters or membrane-related ones.

4. Conclusions

This work combines EIS-DRT in a GDE half-cell as a rapid diagnostic framework to resolve how membranes alter CL properties and interfacial processes. This is also the first time that the contribution of membrane properties on different parts of the total cell resistance has been systematically and quantitatively characterised. By isolating the cathode from full-cell complexity, we show that PEM insertion systematically increases ohmic resistance while directly affecting local proton transfer at the electrode/membrane interface. R_{ct} is strongly influenced by the membrane thickness, while mass transport depends also on polymer chemistry, operating conditions

(current, gas stoichiometry) and CCL. Aquivion Post Coat, in contrast, consistently lowers R_{ct} and R_{mt}, highlighting how ultrathin ionomer films and partially mitigated ionomer through the CL enhance local proton transport and promote a more efficient three-phase boundary formation. For instance, developers can now use this methodology to co-optimize polymer chemistry (e.g., using SSC) to minimize mass transport limitations, while independently engineering its thickness to manage the crucial trade-off between ohmic losses and charge transfer kinetics at the interface.

Unlike PEMFC single-cell studies such as the work of Fortin et al.,[12] where humidified gases and a membrane electrolyte dominate transport, the liquid-acid, non-humidified half-cell environment differs fundamentally from PEMFC operation. The consequence is that this methodology is not a surrogate for full-cell testing but rather a precision diagnostic tool. Consequently, this methodology is not intended as a direct surrogate for full-cell testing, and quantitative comparisons between half-cell and MEA performance are inherently not straightforward. Its primary value lies instead in isolating cathode-side interfacial phenomena under highly reproducible conditions. Within this scope, transferable outcomes include the relative ranking of membrane materials, qualitative trends in DRT peak evolution associated with ORR kinetics and proton accessibility, and the sensitivity of transport- and charge-transfer-related features to membrane chemistry and thickness. These membrane-specific trends provide actionable screening metrics to guide material selection and interface design prior to full-cell validation.

Future studies will extend this approach by systematically varying gas humidification, reactant composition, and operating temperature toward conditions more relevant to PEMFC operation. By correlating the resulting DRT features with post-test cross-sectional and interfacial characterization, the interpretation of low-frequency impedance contributions is further constraint.

Author contributions

Yawen Zhu: conceptualization, methodology, visualization, validation, formal analysis, data curation, writing – original draft. Mena-Alexander Kräenbring: conceptualization, methodology, resources, writing – review & editing. Ivan Radev: conceptualization, writing – review & editing. Ahammed Suhail Odungat: formal analysis, writing – review & editing. Lars Grebener: writing – review & editing. Oliver Pasdag: resources. Thai Binh Nguyen: formal analysis. Doris Segets: conceptualization, supervision, project administration, funding acquisition, writing – review & editing. Fatih Özcan: conceptualization, supervision, project administration, funding acquisition, writing – review & editing.

AI declaration

During the preparation of this work the authors used ChatGPT (GPT-5) in order to improve readability. Before submitting, the authors reviewed and edited the content as needed and take full responsibility for the content of the published article.

Conflicts of interest

There are no conflicts to declare.

Data availability

The definition of I/C ratio in this work (SI 1), FIB-SEM figures of the electrodes (Fig. S1), cross-section of the GDE half-cell setup (Fig. S2) and DRT peak positions (Fig. S3) are shown in supplementary information (SI). See DOI: https://doi.org/10.1039/d5ya00372e.

The data underlying this paper are included as part of the supplementary information (SI) and are available on NOMAD. DOI: https://doi.org/10.17172/NOMAD/2026.03.06-1.

Acknowledgements

Notes and references

1 K. R. Ngoy, V. T. Lukong, K. O. Yoro, J. B. Makambo, N. C. Chukwuati, C. Ibegbulam, O. Eterigho-Ikelegbe, K. Ukoba and T.-C. Jen, Lithium-ion batteries and the future of sustainable energy: A comprehensive review, *Renewable Sustainable Energy Rev.*, 2025, **223**, 115971.

2 H. Heidary, A. El-Kharouf, R. Steinberger-Wilckens, S. Bozorgmehri, M. Salimi and M. Golmohammad, Life cycle assessment of solid oxide fuel cell vehicles in a natural gas producing country; comparison with proton electrolyte fuel cell, battery and gasoline vehicles, *Sustainable Energy Technol. Assess.*, 2023, **59**, 103396.

3 M. Yekini Suberu, M. Wazir Mustafa and N. Bashir, Energy storage systems for renewable energy power sector integration and mitigation of intermittency, *Renewable Sustainable Energy Rev.*, 2014, **35**, 499–514.

4 Y. Qin, Q. Du, M. Fan, Y. Chang and Y. Yin, Study on the operating pressure effect on the performance of a proton exchange membrane fuel cell power system, *Energy Convers. Manage.*, 2017, **142**, 357–365.

5 Y. Zhang, J. Li, L. Ma, W. Cai and H. Cheng, Recent Developments on Alternative Proton Exchange Membranes:

Strategies for Systematic Performance Improvement, *Energy Technol.*, 2015, **3**, 675–691.

6 L. Dubau, L. Castanheira, F. Maillard, M. Chatenet, O. Lottin, G. Maranzana, J. Dillet, A. Lamibrac, J. Perrin, E. Moukheiber, A. ElKaddouri, G. De Moor, C. Bas, L. Flandin and N. Caqué, A review of PEM fuel cell durability: materials degradation, local heterogeneities of aging and possible mitigation strategies, *WIREs Energy Environ.*, 2014, **3**, 540–560.

7 L. Zhang and S. Mukerjee, Investigation of Durability Issues of Selected Nonfluorinated Proton Exchange Membranes for Fuel Cell Application, *J. Electrochem. Soc.*, 2006, **153**, A1062.

8 H. J. Choi, H. J. Choi, J. Kim, H. Choi, C. Chu, I. La, C.-Y. Ahn, H. Shim, O.-H. Kim and Y.-H. Cho, Comparison on the impact of membrane thickness on the performance of proton exchange membrane-based electrochemical devices, *Int. J. Hydrogen Energy*, 2025, **119**, 161–172.

9 S. Cuynet, A. Caillard, J. Bigarré and P. Buvat, Impact of the patterned membrane morphology on PEMFC performances of ultra-low platinum loaded MEAs, *Int. J. Hydrogen Energy*, 2017, **42**, 7974–7985.

10 Y. Tang, A. Kusoglu, A. M. Karlsson, M. H. Santare, S. Cleghorn and W. B. Johnson, Mechanical properties of a reinforced composite polymer electrolyte membrane and its simulated performance in PEM fuel cells, *J. Power Sources*, 2008, **175**, 817–825.

11 N. Ramaswamy, S. Kumaraguru, R. Koestner, T. Fuller, W. Gu, N. Kariuki, D. Myers, P. J. Dudenas and A. Kusoglu, Editors' Choice—Ionomer Side Chain Length and Equivalent Weight Impact on High Current Density Transport Resistances in PEMFC Cathodes, *J. Electrochem. Soc.*, 2021, **168**, 024518.

12 Y. Choi, P. Platzek, J. Coole, S. Buche and P. Fortin, The Influence of Membrane Thickness and Catalyst Loading on Performance of Proton Exchange Membrane Fuel Cells, *J. Electrochem. Soc.*, 2024, **171**, 104507.

13 M. N. Tsampas, A. Pikos, S. Brosda, A. Katsaounis and C. G. Vayenas, The effect of membrane thickness on the conductivity of Nafion, *Electrochim. Acta*, 2006, **51**, 2743–2755.

14 J.-M. Le Canut, R. Latham, W. Mérida and D. A. Harrington, Impedance study of membrane dehydration and compression in proton exchange membrane fuel cells, *J. Power Sources*, 2009, **192**, 457–466.

15 J. Choi, J. Sim, H. Oh and K. Min, Resistance Separation of Polymer Electrolyte Membrane Fuel Cell by Polarization Curve and Electrochemical Impedance Spectroscopy, *Energies*, 2021, **14**, 1491.

16 K. R. Cooper and M. Smith, Electrical test methods for on-line fuel cell ohmic resistance measurement, *J. Power Sources*, 2006, **160**, 1088–1095.

17 P. Choi, J. Kwon, J. Oh, J. Hyun and K. Eom, Comparative analysis of performance decline and anode degradation in polymer electrolyte membrane fuel cells under fuel starvation: A strategy for electrode condition assessment using full electrode equivalent circuit model and anode-separated distribution of relaxation times, *Electrochim. Acta*, 2025, **534**, 146560.

18 S. Li, X. Wei, H. Dai, H. Yuan and P. Ming, Voltammetric and galvanostatic methods for measuring hydrogen crossover in fuel cell, *iScience*, 2022, **25**, 103576.

19 M. Schoemaker, U. Misz, P. Beckhaus and A. Heinzel, Evaluation of Hydrogen Crossover through Fuel Cell Membranes, *Fuel Cells*, 2014, **14**, 412–415.

20 D. Cahan and J. S. Wainright, *AC Impedance Investigations of Proton Conduction in NafionTM*.

21 S. Mikhailenko, M. Guiver and S. Kaliaguine, Measurements of PEM conductivity by impedance spectroscopy, *Solid State Ionics*, 2008, **179**, 619–624.

22 H. Huang, Z. Zhang, C. Xiao, J. Liu, Z. Li, Y. Jiang, L. Wei, T. Zhao, F. Ciucci and L. Zeng, Water Management Fault Diagnosis by Operando Distribution of Relaxation Times Analysis for Anion Exchange Membrane Fuel Cells, *Adv. Sci.*, 2025, **12**, 2505304.

23 P. K. Mohanta, M. S. Ripa, F. Regnet and L. Jörissen, Impact of Membrane Types and Catalyst Layers Composition on Performance of Polymer Electrolyte Membrane Fuel Cells, *ChemistryOpen*, 2020, **9**, 607–615.

24 L. Napoli, J. Franco, H. Fasoli and A. Sanguinetti, Conductivity of Nafion® 117 membrane used in polymer electrolyte fuel cells, *Int. J. Hydrogen Energy*, 2014, **39**, 8656–8660.

25 T. Navessin, S. Holdcroft, Q. Wang, D. Song, Z. Liu, M. Eikerling, J. Horsfall and K. V. Lovell, The role of membrane ion exchange capacity on membrane|gas diffusion electrode interfaces: a half-fuel cell electrochemical study, *J. Electroanal. Chem.*, 2004, **567**, 111–122.

26 B. A. Pinaud, A. Bonakdarpour, L. Daniel, J. Sharman and D. P. Wilkinson, Key Considerations for High Current Fuel Cell Catalyst Testing in an Electrochemical Half-Cell, *J. Electrochem. Soc.*, 2017, **164**, F321–F327.

27 K. Ehelebe, D. Seeberger, M. T. Y. Paul, S. Thiele, K. J. J. Mayrhofer and S. Cherevko, Evaluating Electrocatalysts at Relevant Currents in a Half-Cell: The Impact of Pt Loading on Oxygen Reduction Reaction, *J. Electrochem. Soc.*, 2019, **166**, F1259–F1268.

28 N. Schmitt, M. Schmidt, G. Hübner and B. J. M. Etzold, Oxygen reduction reaction measurements on platinum electrocatalysts in gas diffusion electrode half-cells: Influence of electrode preparation, measurement protocols and common pitfalls, *J. Power Sources*, 2022, **539**, 231530.

29 K. Ehelebe, N. Schmitt, G. Sievers, A. W. Jensen, A. Hrnjić, P. Collantes Jiménez, P. Kaiser, M. Geuß, Y.-P. Ku, P. Jovanovič, K. J. J. Mayrhofer, B. Etzold, N. Hodnik, M. Escudero-Escribano, M. Arenz and S. Cherevko, Benchmarking Fuel Cell Electrocatalysts Using Gas Diffusion Electrodes: Inter-lab Comparison and Best Practices, *ACS Energy Lett.*, 2022, **7**, 816–826.

30 N. Schmitt, M. Schmidt, J. E. Mueller, L. Schmidt, M. Trabold, K. Jeschonek and B. J. M. Etzold, Which insights can gas diffusion electrode half-cell experiments give into activity trends and transport phenomena of membrane electrode assemblies?, *Energy Adv.*, 2023, **2**, 854–863.

31 P. Lauf, V. Lloret, M. Geuß, C. C. Collados, M. Thommes, K. J. J. Mayrhofer, K. Ehelebe and S. Cherevko, Characterization

of Oxygen and Ion Mass Transport Resistance in Fuel Cell Catalyst Layers in Gas Diffusion Electrode Setups, *J. Electrochem. Soc.*, 2023, **170**, 064509.

32 R. Sharma, R. Maurya and S. M. Andersen, True gas phase oxygen reduction reaction (ORR) explorations at the electrolyte/gas interface: A unique screening configuration to study electrode interface structure for PEMFCs, *J. Power Sources*, 2025, **641**, 236841.

33 P. Lauf, A. L. Morales, K. Ehelebe, A. Hutzler, K. J. J. Mayrhofer, V. Lloret and S. Cherevko, Benchmarking Performance and Degradation of Pt Supported on Different Carbons for PEMFC Applications Using Gas Diffusion Electrode Half-Cell, *ACS Appl. Energy Mater.*, 2025, **8**, 7939–7947.

34 E. Tardy, R. Riasse, F. Vandenberghe, F. Druart, M. Chatenet and A. Bonnefont, Understanding the Operation of a Gas Diffusion Electrode Setup for the Oxygen Reduction Reaction: Experiment versus 3D Multiphysics Modeling, *ChemElectroChem*, 2025, **12**, e202500172.

35 L. Grebener, A. S. Odungat, Y. Zhu, O. Pasdag, I. Radev, E. Nürenberg, A. Kubina, V. Peinecke, S. Kohsakowski, D. Segets and F. Özcan, Investigation of fuel cell catalyst dispersion formulations for indirect roll-to-roll fabrication of catalyst coated membranes for proton exchange membrane fuel cells, *J. Power Sources*, 2025, **635**, 236457.

36 L. F. Arenas, G. Hadjigeorgiou, S. Jones, N. Van Dijk, D. Hodgson, A. Cruden and C. Ponce De León, Effect of airbrush type on sprayed platinum and platinum-cobalt catalyst inks: Benchmarking as PEMFC and performance in an electrochemical hydrogen pump, *Int. J. Hydrogen Energy*, 2020, **45**, 27392–27403.

37 M.-A. Kräenbring, L. Wickert, V. Müller, A. Amin, A. Jain, J. T. Kleinhaus, K. Pellumbi, D. Siegmund, F. Özcan, U.-P. Apfel and D. Segets, Emulsion-based electrolytes for sustainable electrocatalytic synthesis and efficient product recovery in zero-gap electrolyzers, *Chem. Eng. J.*, 2025, **523**, 168297.

38 H. J. Cassady, Z. Yang, M. F. Rochow, J. D. Saraidaridis and M. A. Hickner, Crossover Flux and Ionic Resistance Metrics in Polysulfide-Permanganate Redox Flow Battery Membranes, *J. Electrochem. Soc.*, 2024, **171**, 030527.

39 J. Peron, A. Mani, X. Zhao, D. Edwards, M. Adachi, T. Soboleva, Z. Shi, Z. Xie, T. Navessin and S. Holdcroft, Properties of Nafion® NR-211 membranes for PEMFCs, *J. Membr. Sci.*, 2010, **356**, 44–51.

40 R. Loukrakpam, B. Ferreira Gomes, T. Kottakkat and C. Roth, A bird's eye perspective of the measurement of oxygen reduction reaction in gas diffusion electrode half-cell set-ups for Pt electrocatalysts in acidic media, *J. Phys.: Mater.*, 2021, **4**, 044004.

41 T. H. Wan, M. Saccoccio, C. Chen and F. Ciucci, Influence of the Discretization Methods on the Distribution of Relaxation Times Deconvolution: Implementing Radial Basis Functions with DRTtools, *Electrochim. Acta*, 2015, **184**, 483–499.

42 E. Ivers-Tiffée and A. Weber, Evaluation of electrochemical impedance spectra by the distribution of relaxation times, *J. Ceram. Soc. Jpn.*, 2017, **125**, 193–201.

43 S. Litster and G. McLean, PEM fuel cell electrodes, *J. Power Sources*, 2004, **130**, 61–76.

44 T. E. Springer, T. A. Zawodzinski, M. S. Wilson and S. Gottesfeld, Characterization of Polymer Electrolyte Fuel Cells Using AC Impedance Spectroscopy, *J. Electrochem. Soc.*, 1996, **143**, 587–599.

45 A. Weiß, S. Schindler, S. Galbiati, M. A. Danzer and R. Zeis, Distribution of Relaxation Times Analysis of High-Temperature PEM Fuel Cell Impedance Spectra, *Electrochim. Acta*, 2017, **230**, 391–398.

46 D.-H. Kim, H.-S. Jung, D. H. Kim and C. Pak, Using distribution of relaxation times to separate the impedances in the membrane electrode assembly for high-temperature polymer electrolyte membrane fuel cells, *Int. J. Hydrogen Energy*, 2024, **62**, 389–396.

47 D. H. Kim, J. G. Kim, H.-S. Jung and C. Pak, Unveiling the resistance component on fuel cell electrodes by ionic liquid adsorbed PtCo/C catalyst through distribution of relaxation time, *Appl. Surf. Sci.*, 2024, **657**, 159797.

48 M. Loewer, T. Günther, J. Igel, S. Kruschwitz, T. Martin and N. Wagner, Ultra-broad-band electrical spectroscopy of soils and sediments—a combined permittivity and conductivity model, *Geophys. J. Int.*, 2017, **210**, 1360–1373.

49 M. Schalenbach, Y. E. Durmus, H. Tempel, H. Kungl and R.-A. Eichel, The role of the double layer for the pseudo-capacitance of the hydrogen adsorption on platinum, *Sci. Rep.*, 2022, **12**, 3375.

50 H.-S. Jung, S. T. Lee, S.-H. Moon, C. Pak and J.-H. Kim, Integrated MEA for polymer electrolyte membrane fuel cells enabled by freeze–casting and direct membrane deposition, *Chem. Eng. J.*, 2026, **527**, 171993.